CMP06: Effect of Surface Doping on Electronic Structure of Iron Based Superconductors

Candidate No.:1006281 **Project No.:**CMP06 **Supervisor:** Amalia Coldea **Word count:** 4223
(Dated: April 28, 2019)

Understanding superconductivity requires a detailed understanding of the band structure of superconducting materials. This could allow us to engineer these materials to higher critical temperatures. Recent discoveries of enhanced superconductivity below 100K in FeSe monolayer films have sparked much debate as to the cause, however theory has yet to fully explain these findings. In this report, I investigate the effect of surface potassium doping of $FeSe_{1-x}S_x$ by analysing the electronic band structure with Angle Resolved PhotoEmission Spectroscopy (**ARPES**). I extract dispersion peaks from MDCs and I fit them to appropriate curves. I find that hole pockets in the Brillouin zone close up, leaving a single large electron pocket at the M point. Further, I find that under dosing, superconductivity is strongly enhanced with superconductivity below 40K from its pristine value of 8K.

I. INTRODUCTION

Superconductivity was discovered by the physicist Heike Kamerlingh Onnes (1911) [1]. It is characterised by zero electrical resistance and expulsion of magnetic flux (Meissner effect) [2] below a transition temperature T_c. As such, a current set up in a superconductor will remain indefinitely [3]. These effects were first described by the London equations with close comparison to superfluids. A full theory explaining low temperature superconductivity was published in 1957 by Bardeen, Cooper, and Schrieffer (BCS Theory) [4]. However, in 1986, cuprate ceramic materials were discovered with $T_c > 90\,\mathrm{K}$ [5, 6]. These could not be explained by the BCS theory and were named "high-temperature superconductors" to separate them from better understood "classical superconductors". The high-temperature superconductors were of particular interest commercially as they are superconducting at high enough temperature to be cooled by liquid nitrogen, or by liquid helium with comparatively little insulation.

Discovered in 2006, iron-based superconductors are a modern class of high-temperature superconductors where Fe plays a key role in superconductivity [7, 8]. Previous to their discovery, high-temperature superconductors were Cu based [9]. The discovery was surprising as the large magnetic moment of Fe was thought to prevent Cooper pair formation [10]. The new class of high-temperature superconductor provided an opportunity to explore the physics underlying high T_c superconductors in general, an effect that is still yet to be fully explained by theory.

The simplest class of Fe-based superconductors are Fe-chalcogenides [11] such as the layered crystal iron selenide FeSe. Due to their simplicity they are a good target for investigations into the cause of their superconductivity. However, a number of interesting features in variations of this material could provide clues in that search. In bulk FeSe the transition temperature changes from around $9\,\mathrm{K}$ to $38\,\mathrm{K}$ under pressure [12]. Using potassium intercalation between FeSe layers, T_c can be brought above $30\,\mathrm{K}$ [13]. With chemical intercalation and pressure superconductivity reemerges at $T_c = 48\,\mathrm{K}$ [14]. The record for superconductivity in bulk FeSe-based compounds is $T_c = 56\,\mathrm{K}$ [15]. Much higher transition temperatures have been discovered in monolayer films of FeSe on $SrTiO_3$(STO) substrate [16–20] with reported values of T_c above $100\,\mathrm{K}$. This sparked much research into these monolayer films [21]. The high tunability of the transition temperature that can be seen in Figure 1(**a**) makes iron-chalcogenides a first-class tool to investigate enhanced and suppressed superconductivity. Figure 1(**b**) shows the layed structure of FeSe. This layering gives rise to the low dimensionality of the material.

FeSe displays a nematic electronic state from which superconductivity emerges [22]. This nematic transition breaks symmetry between x and y directions of the crystal lattice and reduces the symmetry from tetragonal to orthorhombic. However, this nematic phase can be suppressed by chemical pressure from substitution of Se $\rightarrow$ S [23]. With the nematic state disappearing at $FeSe_{1-x}S_x$ $x \sim 0.18$.

In this report I investigate the suitability of ARPES for analysing the superconductivity of iron chalcogenides and study the changes in superconductivity and electronic structure of $FeSe_{1-x}S_x$ ($x \approx$

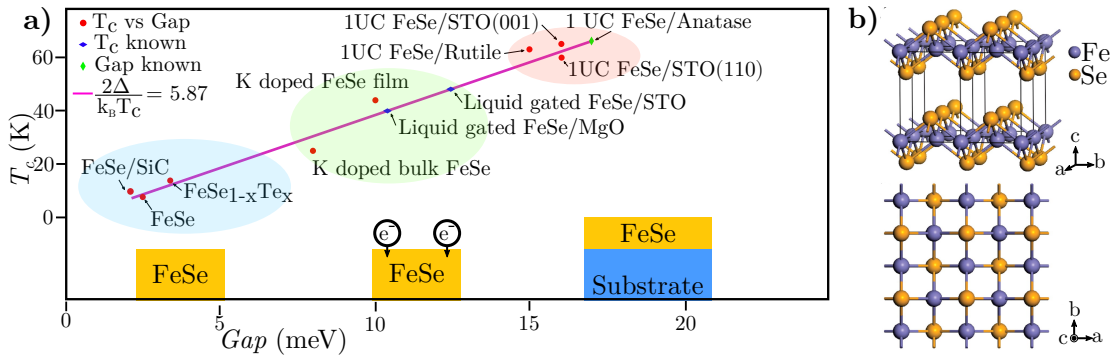

FIG. 1. (**a**) Schematic showing superconducting gap and critical temperature of a number of iron chalcogenide based materials. Adapted from Rebec *et al.* [21]. (**b**) Schematic crystal structure of α-FeSe. Four unit cells are shown to reveal the layered structure. Taken from Hsu *et al.* [24].

0.18) as it is doped in-situ with potassium. I start with an overview of ARPES as an experimental method.

II. ARPES

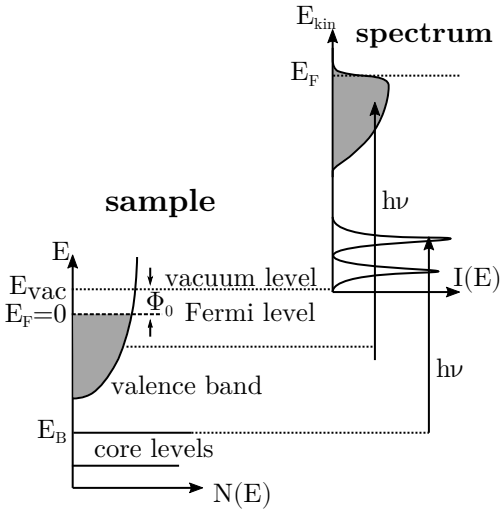

FIG. 2. Schematic view of the photoemission process in the single particle picture. Electrons with binding energy E_B can be excited above the vacuum level E_{vac} by photons with energy $h\nu > E_B + \phi_0$. The photoelectron distribution $I(E_{\text{kin}})$ can be measured by the analyser and is—in first order—an image of the occupied density of electronic states $N(E_B)$ in the sample. Adapted from Reinert and Hüfner [25].

ARPES works from the principle of the photoelectric effect. When electrons in a substance absorb an incident photon, they can gain the energy required to escape the crystal. When they do this, they retain information about their original state such as the momentum in the plane of the crystal surface. The photoelectric effect was first observed by H. Hertz (1887) [26] and explained by Einstein (1905) with the introduction of light quanta [27].

Figure 2 shows a schematic model of the photoemission process. With photoemission, information about the electronic structure of the crystal can be gathered due to the conservation of energy between states. During the photoemission the electron vacuum energy

$$E_{kin} = h\nu + E_B - \phi$$

where ϕ is the material work function. This effect is used to gather information about the electronic density of states in crystals as can be seen in Figure 2. The density of states of the photoelectrons $D(E_{kin})$ as a function of energy will be the same as the electronic density of states of the crystal $D(E_B)$ as a function of energy.

Momentum is also conserved on excitation, in principle allowing the sample momentum to be determined if the photoelectron momentum is resolved. This is the principle of Angle Resolved PhotoEmission Spectroscopy, ARPES. It is important to note however that the work function will cause an acceleration of the photon perpendicular to sample plane upon leaving the crystal which will break conservation of k_z.

The theoretical models of ARPES are summarised in Figure 3(**a**). An accurate description of photoemission requires the 'One Step Model' [29, 30]. This includes photon and photoelectron ef-

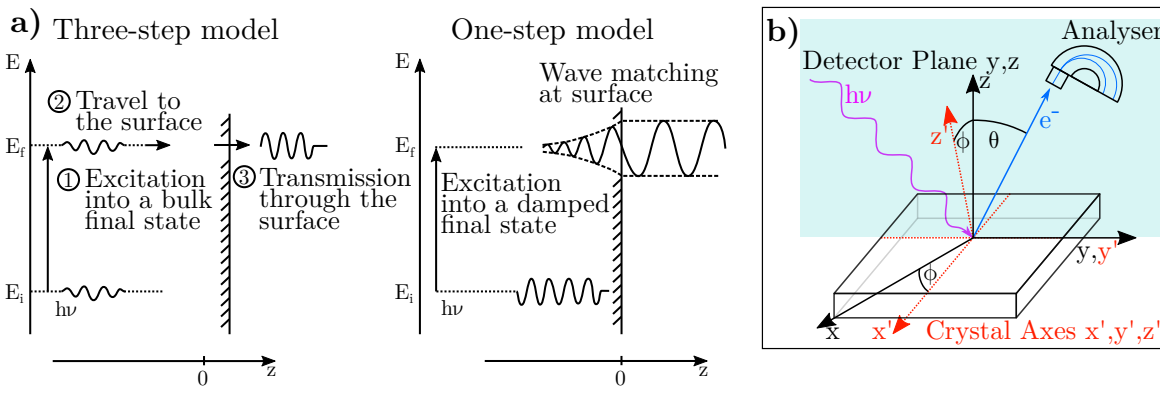

FIG. 3. (**a**) Schematic comparison of the three-step and one-step models of photoemission. Adapted from Hüfner [28]. (**b**) Schematic representation of the experimental setup for ARPES having incident light $h\nu$. The sample coordinates are (x', y', z') while the detector coordinates are (x, y, z). The detector can detect electron momenta in the $y = 0$ plane. Full dispersions are gathered by sweeping ϕ by rotating the sample.

fects together as a single process but is very complex. A simplified theory is the 'Three step model' [31] consisting of distinct processes: I) excitation from initial to bulk final state, II) transmission from bulk to surface, III) escape to vacuum.

On excitation (I), the momentum of the electron is conserved: $\boldsymbol{k}^* = \boldsymbol{k} + \boldsymbol{k}_{photon}$. Scattering in step II could change the momentum $\boldsymbol{k}$ on the way to the surface, however scattering does not prefer any particular angle and so scattered photoelectrons will simply contribute to the background noise. Finally, on leaving the crystal, the work function causes an energy gradient at the surface. This will cause photoelectrons to feel a force towards the crystal plane. This will effectively cause scattering in $\boldsymbol{k}_z$ and remove the ability to resolve $\boldsymbol{k}_z$. However, the in-plane momentum $\boldsymbol{k}_{\|}$ is conserved throughout the process. The primary result of such an analysis is that in a quasi-two dimensional system the photointensity $I(\boldsymbol{k}, \omega)$ is related only to the single particle spectral function $I(\boldsymbol{k}, \omega) = f(\omega)A(\boldsymbol{k}, \omega)$ with a Fermi level cutoff [32].

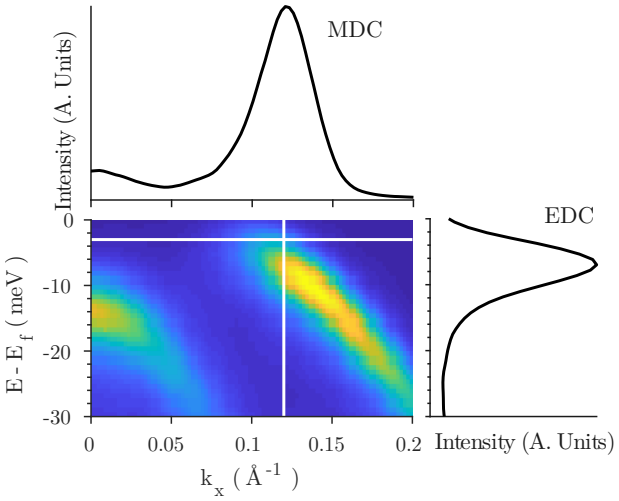

FIG. 4. Energy-momentum distribution of electron intensity. MDC (Momentum Distribution Curve) shows detection intensity at constant energy shown as vertical white line on dispersion. EDC (Energy Distribution Curve) shows detection intensity at constant in-plane momentum k_x shown as horizontal white line on dispersion.

Experimentally, electrons are detected by an analyser with its own work function. An electrical contact between the analyser and the sample aligns their Fermi levels. Energies can be found using a gold powder reference sample at the same constant photon energy. As this is a polycrystalline material, it will have a clear (often weakly momentum dependant) Fermi level that can be used as a reference point for other samples.

Typically, a Hemispherical Deflection Analyser (HDA) is used as the photoelectron analyser. This can resolve momenta in the 'Detector Plane' y,z giving θ and energy from Figure 3. A resolution in $k_{x'}$ can be achieved by rotating the sample in ϕ. There will be a lower resolution in ϕ than in θ. An experiment performed at constant $\phi = 0$ is called a 'cut' and represents a line through the Brillouin zone with energy resolution. Varying ϕ gives an experiment called a 'map' which is a 2D plane through the Brillouin zone (integrated over some range in k_z).

There are a number number of ways of finding

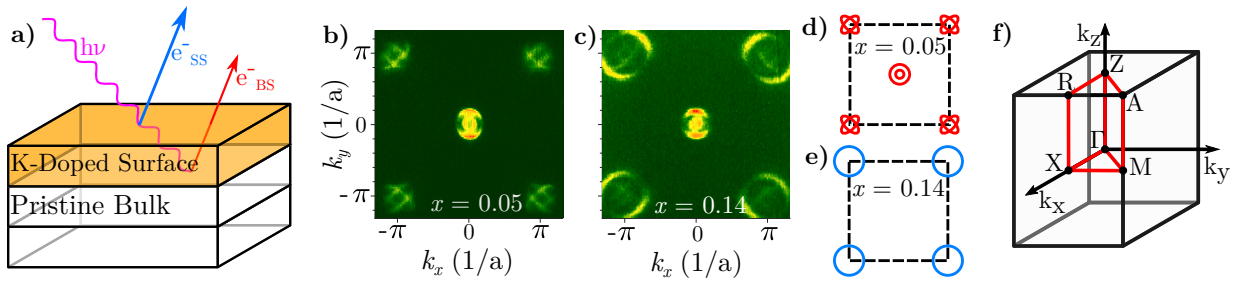

FIG. 5. (**a**) Schematic representation showing incident ARPES photon $h\nu$ probing both surface states (SS) and bulk states (BS) separately. As only the first unit cell is doped by potassium, pristine bulk states can be seen in ARPES data. (**b**,**c**) Maps taken before and after dosing, showing general changes in Fermi surface caused by dosing. (**d**,**e**) A 2D schematic showing the extracted Fermi surface before an after dosing. (**f**) A schematic of the Brillouin zone showing points of high symmetry and symmetry lines in a primitive tetragonal lattice.

peaks in photoemission intensity. Figure 4 shows the two primary methods by which peaks are extracted. MDCs measure photocurrent at constant energy $I_{ph}(E_{MDC}, k)$, while EDCs measure photocurrent at constant in plane momentum $I_{ph}(E, k_{EDC})$. Curves fitted from these can be used to find the peaks which bands can be fitted to to extract macroscopic properties such as effective mass, Fermi velocities, and Fermi wave vectors.

Another macroscopic property that can be extracted is the superconducting gap Δ. BCS theory predicts a DOS at the Fermi level given by the Dynes function [33]. EDCs are most sensitive to this near k_f so typically EDCs taken at k_f are fitted to Dynes function where the gap Δ can be extracted. Often, EDCs are symmetrised so the effects of thermal broadening can be ignored as is shown in Appendix C

III. EFFECT OF K-DOSING OF $FeSe_{1-x}S_x$

The effect of surface doping (dosing) a sample at low temperature is to create a 1u.c. layer of doped material while the bulk remains pristine. While ARPES is sensitive to surface effects, photons are able to penetrate to the second unit cell and beyond. As shown in Figure 5(**a**), ARPES can probe both the doped surface and undoped (pristine) bulk. I would expect the band structure of the bulk crystal to be unchanged by doping and for data from ARPES to show a superposition of doped and undoped bulk states. These bands are effectively from a different crystal and so there should be no hybridisation between these surface state (SS) bands and bulk state (BS) bands. Throughout this report, these unmoving bulk bands will be labeled 'BS' while the changing doped bands will be labeled 'SS'. They will be colour-coded as in Figure 5. As the dosed material is effectively a monolayer, the band structure should become more two-dimensional, with structures at the A and Z points approaching those at the M and Γ points respectively.

Figure 5(**b,c,d,e**) shows the general changes in Fermi surface due to doping. As the material is electron doped the electron pockets grow and the hole pockets shrink. The hole pocket at the Γ point has disappeared, although the superposition of the bulk state still remains. This disappearance represents a Lifshitz transition. A Lifshitz transition occurs when the top or bottom of a band crossed the Fermi level, causing a pocket in the Brillouin zone to open or close. This causes a dramatic change in the Fermi surface, a continuous pocket could break, separate pockets could merge, or pockets could close entirely [34, 35]. This Lifshitz transition is the closing of the hole pocket at the Γ point. This Lifshitz transition is consistent with similar studies and is thought to be a major contributor to changes in the material's physics [36, 37].

Dosing is approximated by measuring the size of the electron pocket at the M point and approximating it as circular. As can be seen in Figure 5(**c,e**) this approximation is good at large dosings. The change in the Fermi surface area as a fraction of the BZ area gives the change in electron density [38–41].

The sample is dosed with an SAES potassium dispenser with the sample held at low temperature ($\sim 10\,\mathrm{K}$). The dispenser is heated in vacuum and

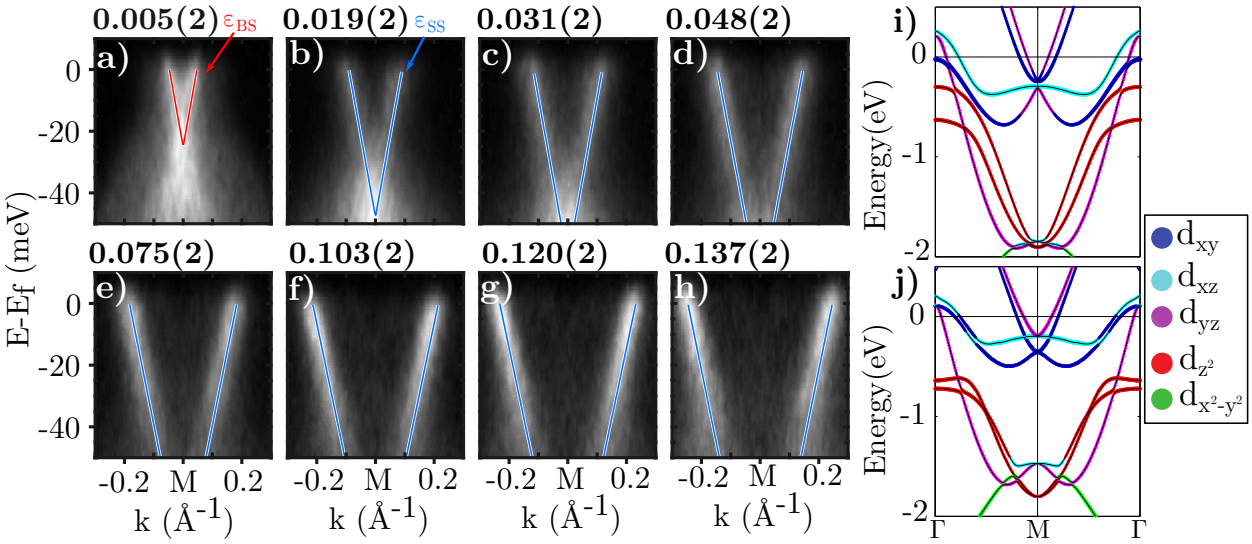

FIG. 6. (**a-h**) Dosing evolution of photointensity cuts measured along the $\Gamma - \mathrm{M} - \Gamma$ direction of $\mathrm{FeSe}_{1-x}\mathrm{S}_x$ $(x \approx 0.18)$. Electron dosing is indicated above each cut in units of electrons per Fe site with estimate of error. Positions of electron bands approximated as linear are overlayed. Pristine band is overlayed in red. Doped bands are overlayed in blue. (**i,j**) Band structure of FeS, and FeSe respectively, calculated with DFT. Taken from Reiss *et al.* [23].

potassium is emitted ballistically due to thermal effects. The sample is then rotated into the path of emission. Potassium is deposited on the sample surface.

Figure 5(**f**) shows high symmetry points in the Brillouin zone of our crystal. The cuts we take are $\Gamma-\mathrm{M}-\Gamma$, $\mathrm{M}-\Gamma-\mathrm{M}$, $\mathrm{Z}-\mathrm{A}-\mathrm{Z}$, and $\mathrm{A}-\mathrm{Z}-\mathrm{A}$. This means that the cut's value $\boldsymbol{k}$ is a value along the line between those points.

A. The changes in electronic structure at the M-point

Next I will compare dispersions at the M point as defined in Figure 5(**f**). Figure 6(**a-h**) show high-symmetry ARPES cuts along the $\Gamma - \mathrm{M} - \Gamma$ line using LV polarisation. In ARPES, spectral weight is highly dependant on matrix element effects. This is because the electrons will interact more strongly with photons in some orbitals than others [42, 43]. Different parts of the band structure are most strongly influenced by different orbitals [23]. The most strongly contributing orbital is called the orbital character which is very momentum dependant in FeSe [22]. In this geometry, the spectral weight is dominated by the single ϵ band with d_{yz} character. The δ band with d_{xy} orbital character that can be seen in Figure 6(**i,j**) is not visible. The single band seen is the ϵ_{SS} electron band. The figure shows changes in that band's dispersion as a function of dosing. The intensity of ϵ_{BS} is much lower if present at all, in significant contrast to the bands α_{BS} and β_{BS} near the Γ point. This could be explained by the increased distance through the surface layer due to a shallower angle of incidence of probing photon, resulting in both stronger probing of surface layer and less intensity reaching the bulk. A check of this would be to investigate the relative intensities at $\Gamma_{1,1}$ and $\Gamma_{1,0}$, in the adjacent Brillouin zones, to establish how these intensities change with angle. It could however be evidence that this M point electron band is more sensitive to surface effects.

Additionally, these can be compared to band structure calculations seen in Figure 6(**i,j**). These calculations are for FeS and FeSe. As $\mathrm{FeSe}_{1-x}\mathrm{S}_x$ $(x \approx 0.18)$ is very strongly correlated these band structures have to be renormalised to be compared quantitatively. This means the curves have to be rescaled to roughly match experimental data. The renormalisation factor is typically ~ 3 [44–46]. However, this factor is highly dependant on which particular material is being studied and on the orbital character [47]. Qualitatively I can see that in the absence of correlations at high binding energies we would expect the Fermi velocity of the

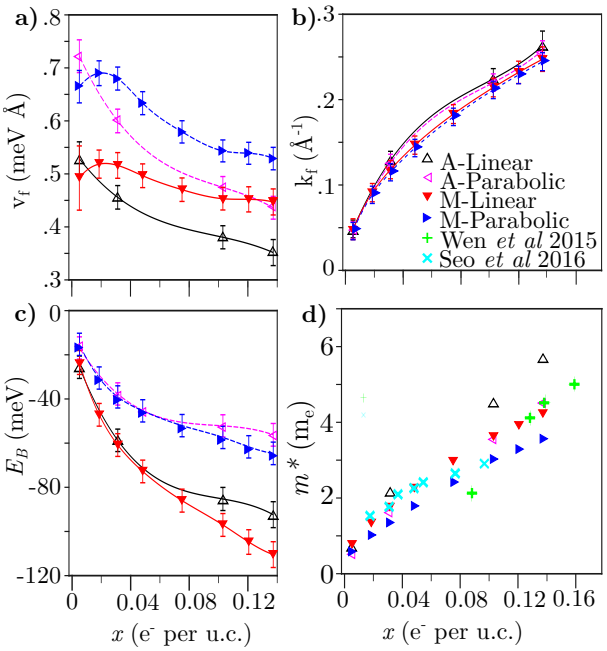

FIG. 7. Dosing evolution of extracted parameters for the ϵ_{SS} band near the M point and the A point for $FeSe_{1-x}S_x$ ($x \approx 0.18$) produced by fitting parabolic and linear dispersion relations along the $\Gamma - M - \Gamma$ and $Z - A - Z$ lines. Masses are defined in Appendix B. (**d**) also contains electron mass data from Seo *et al.* [37], Wen *et al.* [48] with dosing values corrected for consistent units. A smoothing spline in drawn through the points as a guide to the eye.

ϵ to stay approximately constant.b

As you can see in Figure 7(**b**), the size of the electron pocket increases by a factor of 5, from $0.05\,\text{Å}^{-1}$ to $0.25\,\text{Å}^{-1}$. This increase is matched within error by an increase in the size of the electron pocket at the A point. This shows the material remains very two dimensional in it's structure as the Fermi surface is effectively two dimensional. It is with this value $k_f(M)$ that we calculate the level of dosing.

The effective masses m^* of the electron pocket can be seen in Figure 7(**d**). These masses are significantly enhanced from their pristine value of $\sim 0.5\,m_e$ to a highly doped value of $\sim 4.0\,m_e$. When these data are compared with similar studies of FeSe at the same dosing levels derived from the size of the electron pocket, the masses are consistent [37, 48]. For the parabolic fit, effective mass is defined by the second derivative ($E = \frac{\hbar^2}{2m^*}k^2$), for the linear fit, mass is defined by the Fermi velocity ($m^* = \frac{k_f}{v_f}$) as shown in Appendix B. The much larger effective mass is partly due to an increased k_f but also suggests strongly enhanced electron correlations. One possible source of these is 2D confinement of electrons due to the surface layer. However, a recent theory paper suggests electric fields caused by potassium ions on the surface of the material could play an important part in enhanced correlations [49]. This enhancement varies with the orbital character of the band and is largest in d_{xy}.

Figure 7(**a**) shows extracted Fermi velocities v_f along the $\Gamma - M - \Gamma$ and $Z - A - Z$ cuts with both direct measurement (linear fit) and extracted from a parabolic fit of the dispersions. At low dosing, for both methods of extracting the value, the Fermi velocity along $\Gamma - M - \Gamma$ is roughly equal to that along $Z - A - Z$ at $v_f = 0.55\,\text{meV Å}$. As dosing increases, the Fermi velocity decreases and values along $\Gamma - M - \Gamma$ diverge from those along $Z - A - Z$, reaching $0.50\,\text{meV Å}$ near the M point and $0.38\,\text{meV Å}$ near the A point when measured directly. The divergence brings into doubt the idea that the material is acting more two dimensional with dosing than without. However, the decrease in Fermi velocity supports the conclusion that electronic correlations are increasing. This decrease in Fermi velocity cannot be explained by a rigid shift in binding energy as can be seen in Figure 6(**i,j**).

B. The changes in electronic structure at the Γ-point

Figure 8 shows high-symmetry ARPES cuts taken along the $M - \Gamma - M$ line near the Γ point using LH polarisation as a function of dosing. From these cuts I took MDCs and extracted the peaks. Overlaid are parabolic fits to these MDC peaks. The bulk state bands α_{BS} and β_{BS} as defined in Figure 8 are overlaid in red while the surface state bands α_{SS} and β_{SS} , overlaid in blue, can be seen to shift towards higher binding energies as dosing increases. The lack of separation between the bulk and surface bands makes extracting peaks from MDCs much more complex.

Figure 9 shows extracted values for the minimum binding energy E_B and effective mass m^* for the α and β bands. Firstly I observe the hole pocket quickly closes, representing a Lifshitz transition consistent with literature [36] leaving just the electron pocket at M. The result is the new Fermi surface con-

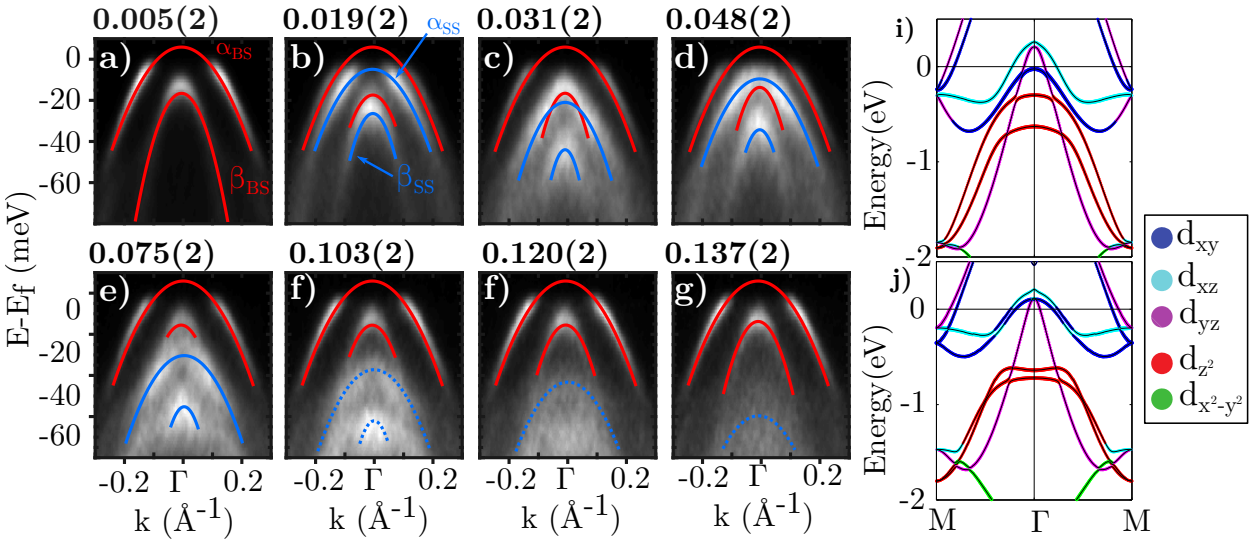

FIG. 8. (**a-h**) Dosing evolution of photointensity cuts measured along the M − Γ − M direction of $FeSe_{1-x}S_x$ ($x \approx 0.18$). Electron dosing is indicated above each cut in units of electrons per Fe Site with estimate of error. Positions of hole bands approximated as parabolic are overlayed. Bulk state bands are shown in red. Surface state bands are shown in blue. Solid lines mark bands that were fitted with MDCs and EDCs. Dashed lines are guides to the eye. (**i,j**) Band structure of FeS, and FeSe respectively, calculated with DFT. Taken from Reiss *et al.* [23].

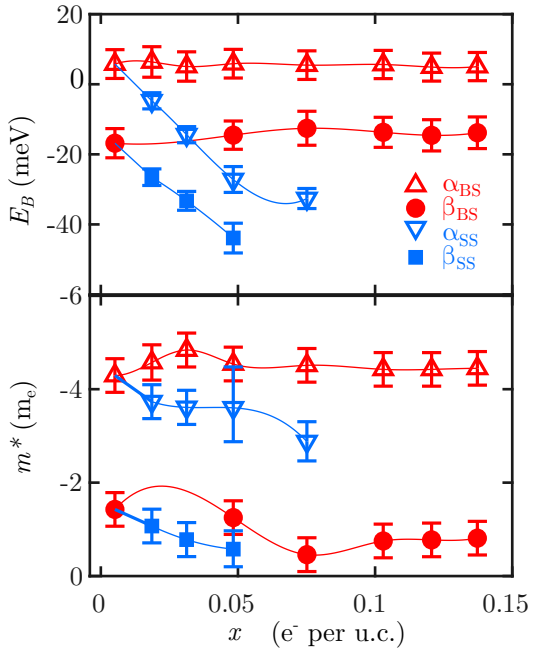

FIG. 9. Dosing evolution of extracted parameters for the α and β bands near the Γ point for $FeSe_{1-x}S_x$ ($x \approx 0.18$) produced by fitting parabolas to MDC peaks. The bands each curve represents is indicated on the right side of graph. A smoothing spline in drawn through the points as a guide to the eye.

tains only electron pockets.

Figure 9(**a**) shows the drop in binding energy of the bands α and β as a function of dosing. The increase in binding energy is expected by traditional band theory as we are electron doping the crystal. The large binding energy of the entire band means that it is only weakly probed by my ARPES setup, decreasing the signal to noise ration as well as causing significant broadening.

The change in effective mass as a function of dosing can be seen in Figure 9(**b**). The values for α_{BS} and β_{BS} stay constant as dosing increases. This supports my hypothesis that they are dispersions from the pristine bulk. For α_{SS} and β_{SS} the magnitude of effective masses drops slightly with dosing. This would not be expected with increasing electronic correlations, however these bands have a different orbital character to ϵ and so different correlations [49].

C. Superconductivity before and after dosing

I will now investigate changes in superconductivity parameters that can be seen in Figure 10. (**a,b**) show symmetrised dispersions at high and low temperatures. This shows the opening of the gap and

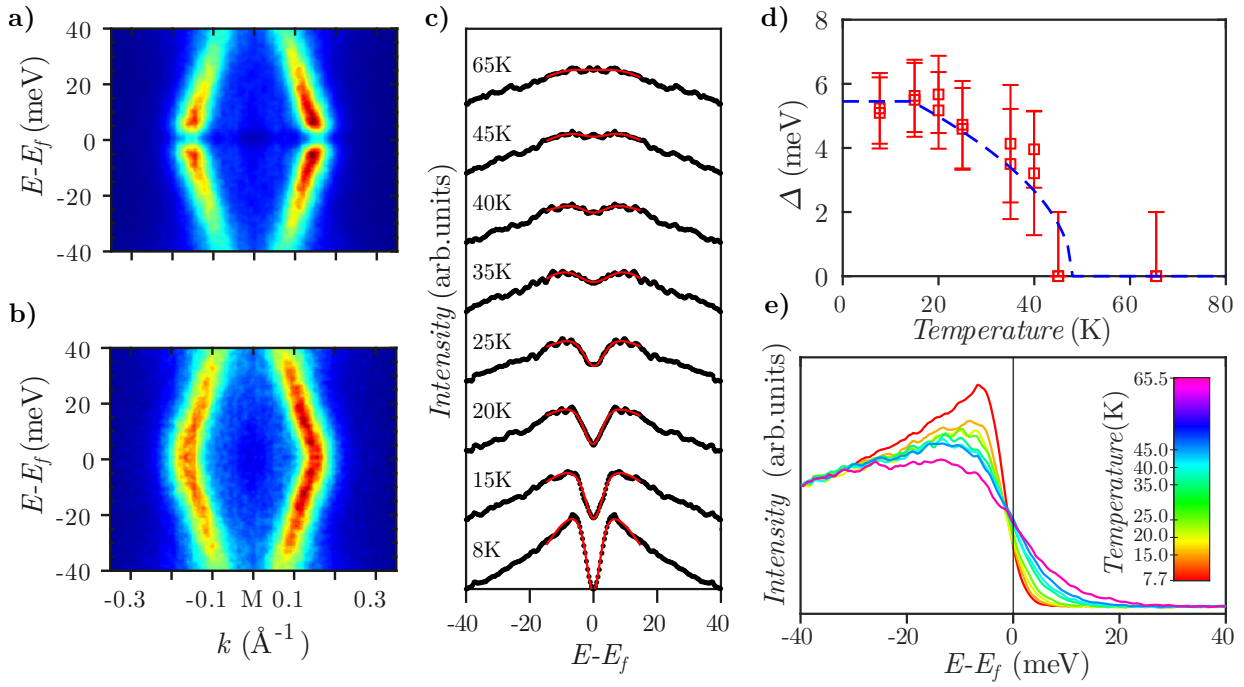

FIG. 10. (**a,b**) Symmetrised dispersions of bands along line $\Gamma - \mathrm{M} - \Gamma$ at 8 K and 66 K respectively for potassium dosed $FeSe_{1-x}S_x\,(x \approx 0.18)$. (**c**) Temperature variation of integrated symmetrised EDCs at the k_f point of the electron Fermi surface around the M point. The red curves represent a fit of the data with a phenomenological model of high-temperature superconductivity. The temperature is indicated above the respective curve. (**d**) Temperature evolution of extracted superconducting gaps Δ with a BCS fit. (**e**) Temperature evolution of integrated EDCs taken at k_f. The temperature of each EDC is shown on the colourbar.

the back-bending of the dispersions below the critical temperature. Figure 10(**c**) shows symmetrised EDCs at k_f. As temperature decreases, a gap opens up with Dynes quasiparticle peaks either side [50]. A notably important parameter is the superconducting gap Δ [51] which is extracted by fitting the data. For my fitting procedure I used a phenomenological model of the gap [52] convolved with my experimental resolution as seen in Appendix D. Figure 10(**d**) shows extracted values for the gap as a function of temperature. The gap decreases near the critical temperature. From these data I extract a low-temperature gap Δ of $5.5(10)\,\mathrm{meV}$ and a critical temperature T_c of $\sim 40(10)\,\mathrm{K}$. Figure 10(**e**) shows EDCs at the k_f point as a function of temperature. At low temperature there is a clear formation of the Bogoliubov peak [53] which is indicative of a superconducting state as it shows formation of Cooper pairs.

My sample's transition temperature of $\sim 40\,\mathrm{K}$ is a large enhancement over the bulk value of 8K. Other studies of K-dosing bulk FeSe gave a superconducting gap of $4.2\,\mathrm{meV}$ with a critical temperature of $\sim 20\,\mathrm{K}$[37]. My value for $FeSe_{1-x}S_x\,(x \approx 0.18)$ has a slightly larger gap of $5.5\,\mathrm{meV}$ but a much larger transition temperature. My sample's stronger superconductivity could be that it is closer to optimal dosing or an effect caused by the Se $\rightarrow$ S substitution. This value is still much less than can be seen in FeSe monolayers with critical temperatures ranging from $50\,\mathrm{K}$ to $100\,\mathrm{K}$ [16–18, 54–56]. These monolayer substances are heavily electron doped by the substrate [57, 58] and so will be affected by some of the same effects caused by electron doping in my sample.

IV. SUMMARY AND FUTURE WORK

By doping the surface of $FeSe_{1-x}S_x$ with potassium I investigated the changes in electronic structure ans superconductivity at the high symmetry points. The first order change of a rigid shift in binding energy is clear at all points in k-space studied. I further analysed the changes of different parameters

such as effective mass m^*, Fermi velocity higher order effects of changes in the shape of the electronic structure are much harder to analyse and quantify but evidence of them can be seen in the changes in effective mass of the bands α_{SS} and β_{SS}. Of critical importance is the ϵ_{SS} band, as this is the only band that crosses the Fermi level. This band shows a ~ 4 fold increase in both effective mass and k_f. This large electron pocket is the only carrier pocket in the doped material and so must be significant. In order to identify an accurate measure of correlations, the gap between the bottom of this band and the top of the band below could be used, with a growing gap implying an increased off diagonal element in the Hamiltonian, and so stronger correlation effects. Correlations can also be probed by accurately measuring the width of the Lorentzian peaks [45, 59] as this gives us the self-energy from the spectral function in Appendix D.

This study has given us further insight into the rich phase diagram of iron chalcogenides, demonstrating that superconductivity is enhanced by a factor of ~ 4 at optimal dosing to a T_c of $\sim 40\,\mathrm{K}$. This superconductivity also exists despite the much suppressed nematic phase.

Other studies on FeSe have linked the Lifshitz transition to an increase in superconductivity and identified a second transition [36] occurring at higher dosings, also at the Γ point and linked it to higher superconductivity still. It would be informative to identify if this occurs in $\mathrm{FeSe}_{1-x}\mathrm{S}_x\,(x \approx 0.18)$ and the increase in T_c is similarly linked by taking more data at even higher levels of dosing. Much higher critical temperatures have been found in FeSe monolayers than even surface doped bulk [16–20]. It would be interesting to investigate superconductivity and band structure of $\mathrm{FeSe}_{1-x}\mathrm{S}_x\,(x \approx 0.18)$ thin films and monolayers to compare them to the bulk and FeSe.

[1] R. de Bruyn Ouboter, "Heike kamerlingh onnes's discovery of superconductivity," Scientific American **276**, 98–103 (1997).

[2] W. Meissner and R. Ochsenfeld, "Ein neuer effekt bei eintritt der supraleitfähigkeit," Naturwissenschaften **21**, 787–788 (1933).

[3] F. London, H. London, and F. A. Lindemann, "The electromagnetic equations of the supraconductor," Proceedings of the Royal Society of London. Series A - Mathematical and Physical Sciences **149**, 71–88 (1935).

[4] J. Bardeen, L. N. Cooper, and J. R. Schrieffer, "Theory of superconductivity," Physical Review **108**, 1175–1204 (1957).

[5] J. G. Bednorz and K. A. Müller, "Possible hight c superconductivity in the ba- la- cu- o system," Zeitschrift für Physik B Condensed Matter **64**, 189–193 (1986).

[6] M.-K. Wu, J. R. Ashburn, C. Torng, P. H. Hor, R. L. Meng, L. Gao, Z. J. Huang, Y. Wang, and a. Chu, "Superconductivity at 93K in a new mixed-phase Y-Ba-Cu-O compound system at ambient pressure," Physical Review Letters **58**, 908 (1987).

[7] Y. Kamihara, H. Hiramatsu, M. Hirano, R. Kawamura, H. Yanagi, T. Kamiya, and H. Hosono, "Iron-based layered superconductor: LaOFeP," Journal of the American Chemical Society **128**, 10012–10013 (2006).

[8] Y. Kamihara, T. Watanabe, M. Hirano, and H. Hosono, "Iron-based layered superconductor $\mathrm{La}[\mathrm{O}_{1-x}\mathrm{F}_x]\mathrm{FeAs}(x = 0.05 - 0.12)$ with T_c = 26K," Journal of the American Chemical Society **130**, 3296–3297 (2008).

[9] K. Takada, H. Sakurai, E. Takayama-Muromachi, F. Izumi, R. A. Dilanian, and T. Sasaki, "Superconductivity in two-dimensional CoO_2 layers," Nature **422**, 53 EP – (2003).

[10] C. Day, "Iron-based superconductors," Physics Today **62**, 36–40 (2009).

[11] Y. Mizuguchi and Y. Takano, "Review of fe chalcogenides as the simplest fe-based superconductor," Journal of the Physical Society of Japan **79**, 102001 (2010).

[12] S. Medvedev, T. M. McQueen, I. A. Troyan, T. Palasyuk, M. I. Eremets, R. J. Cava, S. Naghavi, F. Casper, V. Ksenofontov, G. Wortmann, and C. Felser, "Electronic and magnetic phase diagram of $\beta - \mathrm{Fe}_{1.01}\mathrm{Se}$ with superconductivity at 36.7K under pressure," Nature Materials **8**, 630 EP – (2009).

[13] J. Guo, S. Jin, G. Wang, S. Wang, K. Zhu, T. Zhou, M. He, and X. Chen, "Superconductivity in the iron selenide $\mathrm{K}_x\mathrm{Fe}_2\mathrm{Se2}(0 < x < 1.0)$," Physical Review B **82**, 180520 (2010).

[14] L. Sun, X.-J. Chen, J. Guo, P. Gao, Q.-Z. Huang, H. Wang, M. Fang, X. Chen, G. Chen, Q. Wu, C. Zhang, D. Gu, X. Dong, L. Wang, K. Yang, A. Li, X. Dai, H.-k. Mao, and Z. Zhao, "Re-emerging superconductivity at 48K in iron chalcogenides," Na-

ture **483**, 67 EP – (2012).

[15] G. Wu, Y. L. Xie, H. Chen, M. Zhong, R. H. Liu, B. C. Shi, Q. J. Li, X. F. Wang, T. Wu, Y. J. Yan, J. J. Ying, and X. H. Chen, "Superconductivity at 56K in samarium-doped SrFeAsF," Journal of Physics: Condensed Matter **21**, 142203 (2009).

[16] L. Sun, X.-J. Chen, J. Guo, P. Gao, Q.-Z. Huang, H. Wang, M. . J. Fang, D. Liu, W. Zhang, D. Mou, J. He, Y.-B. Ou, Q.-Y. Wang, Z. Li, L. Wang, L. Zhao, S. He, Y. Peng, X. Liu, C. Chen, L. Yu, G. Liu, X. Dong, J. Zhang, C. Chen, Z. Xu, J. Hu, X. Chen, X. Ma, Q. Xue, X. J. Zhou, X. Chen, G. Chen, Q. Wu, C. Zhang, D. Gu, L. Wang, K. Yang, A. Li, X. Dai, H.-k. Mao, and Z. Zhao, "Electronic origin of high-temperature superconductivity in single-layer FeSe superconductor," Nature Communications **3**, 931 EP – (2012).

[17] Q.-Y. Wang, Z. Li, W.-H. Zhang, Z.-C. Zhang, J.-S. Zhang, W. Li, H. Ding, Y.-B. Ou, P. Deng, K. Chang, J. Wen, C.-L. Song, K. He, J.-F. Jia, S.-H. Ji, Y.-Y. Wang, L.-L. Wang, X. Chen, X.-C. Ma, and Q.-K. Xue, "Interface-induced high-temperature superconductivity in single unit-cell FeSe films on $SrTiO_3$," Chinese Physics Letters **29**, 037402 (2012).

[18] J.-F. Ge, Z.-L. Liu, C. Liu, C.-L. Gao, D. Qian, Q.-K. Xue, Y. Liu, and J.-F. Jia, "Superconductivity above 100K in single-layer FeSe films on doped $SrTiO_3$," Nature Materials **14**, 285 EP – (2014).

[19] P. Zhang, X.-L. Peng, T. Qian, P. Richard, X. Shi, J.-Z. Ma, B. Fu, Y.-L. Guo, Z. Han, S. Wang, *et al.*, "Observation of high-T_c superconductivity in rectangular FeSe/SrTiO 3 (110) monolayers," Physical Review B **94**, 104510 (2016).

[20] J. Lee, F. Schmitt, R. Moore, S. Johnston, Y.-T. Cui, W. Li, M. Yi, Z. Liu, M. Hashimoto, Y. Zhang, *et al.*, "Interfacial mode coupling as the origin of the enhancement of T_c in FeSe films on $SrTiO_3$," Nature **515**, 245 (2014).

[21] S. N. Rebec, T. Jia, C. Zhang, M. Hashimoto, D.-H. Lu, R. G. Moore, and Z.-X. Shen, "Coexistence of replica bands and superconductivity in FeSe monolayer films," Physical Review Letters **118**, 067002 (2017).

[22] M. D. Watson, T. K. Kim, A. A. Haghighirad, N. R. Davies, A. McCollam, A. Narayanan, S. F. Blake, Y. L. Chen, S. Ghannadzadeh, A. J. Schofield, M. Hoesch, C. Meingast, T. Wolf, and A. I. Coldea, "Emergence of the nematic electronic state in FeSe," Physical Review B **91**, 155106 (2015).

[23] P. Reiss, M. Watson, T. Kim, A. Haghighirad, D. Woodruff, M. Bruma, S. Clarke, and A. Coldea, "Suppression of electronic correlations by chemical pressure from FeSe to FeS," Physical Review B **96**, 121103 (2017).

[24] F.-C. Hsu, J.-Y. Luo, K.-W. Yeh, T.-K. Chen, T.-W. Huang, P. M. Wu, Y.-C. Lee, Y.-L. Huang, Y.-Y. Chu, D.-C. Yan, and M.-K. Wu, "Superconductivity in the PbO-type structure α-FeSe," Proceedings of the National Academy of Sciences **105**, 14262–14264 (2008).

[25] F. Reinert and S. Hüfner, "Photoemission spectroscopy—from early days to recent applications," New Journal of Physics **7**, 97 (2005).

[26] H. Hertz, "Ueber einen einfluss des ultravioletten lichtes auf die electrische entladung," Annalen der Physik **267**, 983–1000 (1887).

[27] A. Einstein, "Über einen die erzeugung und verwandlung des lichtes betreffenden heuristischen gesichtspunkt," Annalen der Physik **322**, 132–148 (1905).

[28] S. Hüfner, *Photoelectron spectroscopy: principles and applications* (Springer Science & Business Media, 2013).

[29] J. Minar, "13 theoretical description of arpes: The one-step model," DMFT at 25: Infinite Dimensions (2014).

[30] G. Mahan, "Theory of photoemission in simple metals," Physical Review B **2**, 4334 (1970).

[31] A. Damascelli, "Probing the electronic structure of complex systems by ARPES," Physica Scripta **2004**, 61 (2004).

[32] M. Randeria, H. Ding, J.-C. Campuzano, A. Bellman, G. Jennings, T. Yokoya, T. Takahashi, H. Katayama-Yoshida, T. Mochiku, and K. Kadowaki, "Momentum distribution sum rule for angle-resolved photoemission," Physical Review Letters **74**, 4951–4954 (1995).

[33] D. Evtushinsky, *Physical properties of layered superconductors from angle-resolved photoemission spectroscopy (ARPES)*, Ph.D. thesis, Saechsische Landesbibliothek-Staats-und Universitaetsbibliothek Dresden (2011).

[34] I. Lifshitz *et al.*, "Anomalies of electron characteristics of a metal in the high pressure region," Soviet Physics Journal of Experimental and Theoretical Physics **11**, 1130–1135 (1960).

[35] G. Volovik, "Topological lifshitz transitions," Low Temperature Physics **43**, 47–55 (2017).

[36] X. Shi, Z.-Q. Han, X.-L. Peng, P. Richard, T. Qian, X.-X. Wu, M.-W. Qiu, S. C. Wang, J. P. Hu, Y.-J. Sun, and H. Ding, "Enhanced superconductivity accompanying a Lifshitz transition in electron-doped FeSe monolayer," Nature Communications **8**, 14988 EP – (2017).

[37] J. J. Seo, B. Y. Kim, B. S. Kim, J. K. Jeong, J. M. Ok, J. S. Kim, J. D. Denlinger, S.-K. Mo, C. Kim, and Y. K. Kim, "Superconductivity below 20K in heavily electron-doped surface layer of FeSe bulk crystal," Nature Communications **7**, 11116 EP –

(2016).

[38] J. M. Luttinger, "Fermi surface and some simple equilibrium properties of a system of interacting fermions," Physical Review **119**, 1153–1163 (1960).

[39] J. M. Luttinger and J. C. Ward, "Ground-state energy of a many-fermion system. ii," Physical Review **118**, 1417–1427 (1960).

[40] B. Farid, "On the Luttinger theorem concerning number of particles in the ground states of systems of interacting fermions," arXiv preprint arXiv:0711.0952 (2007).

[41] A. M. Tsvelik, *Quantum field theory in condensed matter physics* (Cambridge Univ. Press, 2006).

[42] X.-P. Wang, P. Richard, Y.-B. Huang, H. Miao, L. Cevey, N. Xu, Y.-J. Sun, T. Qian, Y.-M. Xu, M. Shi, J.-P. Hu, X. Dai, and H. Ding, "Orbital characters determined from fermi surface intensity patterns using angle-resolved photoemission spectroscopy," Physical Review B **85**, 214518 (2012).

[43] Y. Zhang, C. He, Z. Ye, J. Jiang, F. Chen, M. Xu, Q. Ge, B. Xie, J. Wei, M. Aeschlimann, *et al.*, "Symmetry breaking via orbital-dependent reconstruction of electronic structure in detwinned nafeas," Physical Review B **85**, 085121 (2012).

[44] S. V. Borisenko, V. B. Zabolotnyy, D. V. Evtushinsky, T. K. Kim, I. V. Morozov, A. N. Yaresko, A. A. Kordyuk, G. Behr, A. Vasiliev, R. Follath, and B. Büchner, "Superconductivity without nesting in LiFeAs," Physical Review Letters **105**, 067002 (2010).

[45] M. D. Watson, S. Backes, A. A. Haghighirad, M. Hoesch, T. K. Kim, A. I. Coldea, and R. Valentí, "Formation of hubbard-like bands as a fingerprint of strong electron-electron interactions in fese," Physical Review B **95**, 081106 (2017).

[46] D. Evtushinsky, A. Yaresko, V. Zabolotnyy, J. Maletz, T. Kim, A. Kordyuk, M. Viazovska, M. Roslova, I. Morozov, R. Beck, *et al.*, "Anomalous high-energy electronic interaction in iron-based superconductor," arXiv preprint arXiv:1409.1537 (2014).

[47] Z. Yin, K. Haule, and G. Kotliar, "Kinetic frustration and the nature of the magnetic and paramagnetic states in iron pnictides and iron chalcogenides," Nature Materials **10**, 932 (2011).

[48] C. H. P. Wen, H. C. Xu, C. Chen, Z. C. Huang, X. Lou, Y. J. Pu, Q. Song, B. P. Xie, M. Abdel-Hafiez, D. A. Chareev, A. N. Vasiliev, R. Peng, and D. L. Feng, "Anomalous correlation effects and unique phase diagram of electron-doped FeSe revealed by photoemission spectroscopy," Nature Communications **7**, 10840 EP – (2016).

[49] Y. W. Choi and H. J. Choi, "Role of electric fields on enhanced electron correlation in surface-doped FeSe," Physical Review Letters **122**, 046401 (2019).

[50] R. C. Dynes, V. Narayanamurti, and J. P. Garno, "Direct measurement of quasiparticle-lifetime broadening in a strong-coupled superconductor," Physical Review Letters **41**, 1509–1512 (1978).

[51] P. Richard, T. Qian, and H. Ding, "ARPES measurements of the superconducting gap of Fe-based superconductors and their implications to the pairing mechanism," Journal of Physics: Condensed Matter **27**, 293203 (2015).

[52] M. Norman, M. Randeria, H. Ding, and J. Campuzano, "Phenomenology of the low-energy spectral function in high-T_c superconductors," Physical Review B **57**, R11093 (1998).

[53] N. N. Bogolyubov, "On the theory of superfluidity," Izv. Akad. Nauk Ser. Fiz. **11**, 23–32 (1947).

[54] Z. Wen-Hao, S. Yi, Z. Jin-Song, L. Fang-Sen, G. Ming-Hua, Z. Yan-Fei, Z. Hui-Min, P. Jun-Ping, X. Ying, W. Hui-Chao, *et al.*, "Direct observation of high-temperature superconductivity in one-unit-cell FeSe films," Chinese Physics Letters **31**, 017401 (2014).

[55] L. Deng, B. Lv, Z. Wu, Y. Xue, W. Zhang, F. Li, L. Wang, X. Ma, Q. Xue, and C. Chu, "Meissner and mesoscopic superconducting states in 1-4 unit-cell FeSe films," Physical Review B **90**, 214513 (2014).

[56] X. Liu, D. Liu, W. Zhang, J. He, L. Zhao, S. He, D. Mou, F. Li, C. Tang, Z. Li, *et al.*, "Dichotomy of the electronic structure and superconductivity between single-layer and double-layer FeSe/$SrTiO_3$ films," Nature Communications **5**, 5047 (2014).

[57] S. He, J. He, W. Zhang, L. Zhao, D. Liu, X. Liu, D. Mou, Y.-B. Ou, Q.-Y. Wang, Z. Li, *et al.*, "Phase diagram and high temperature superconductivity at 65K in tuning carrier concentration of single-layer FeSe films," arXiv preprint arXiv:1207.6823 (2012).

[58] S. Tan, Y. Zhang, M. Xia, Z. Ye, F. Chen, X. Xie, R. Peng, D. Xu, Q. Fan, H. Xu, *et al.*, "Interface-induced superconductivity and strain-dependent spin density waves in FeSe/$SrTiO_3$ thin films," Nature Materials **12**, 634 (2013).

[59] R. Comin and A. Damascelli, "ARPES: A probe of electronic correlations," in *Strongly Correlated Systems* (Springer, 2015) pp. 31–71.

Appendix A: ARPES coordinate transformations

The coordinate transformations used in converting from angular to Cartesian data are:

$$|\boldsymbol{k}| = \sqrt{2m_e E_{vac}} \tag{A1a}$$
$$k_x = |\boldsymbol{k}| \cos\theta \sin\phi \tag{A1b}$$
$$k_y = |\boldsymbol{k}| \cos\theta \sin\phi \tag{A1c}$$

Appendix B: Definition of Effective Masses

For a circular electron band:

$$A_k = \pi k_f^2 \tag{B1a}$$
$$m^*_{\text{CR}} = \frac{\hbar^2}{2\pi}\frac{\partial A_k}{\partial \epsilon} \tag{B1b}$$
$$= \hbar^2 \frac{k_f}{v_f} \tag{B1c}$$

For a parabolic fit:

$$\epsilon = \frac{1}{2m^*}\hbar^2 k^2 \tag{B2a}$$
$$\implies m^* = m^*_{\text{CR}} \tag{B2b}$$

Appendix C: EDC Symmetrization

$$E_\pm(k) = \pm\sqrt{\epsilon(k)^2 + \Delta(k)^2} \tag{C1}$$
$$A(\boldsymbol{k},\omega) = \frac{1}{\pi}\left\{\frac{|u_k|^2\Sigma''}{[\omega - E(k)]^2 + \Sigma''^2} + \frac{|v_k|^2\Sigma''}{[\omega + E(k)]^2 + \Sigma''^2}\right\} \tag{C2}$$
$$|u_k|^2 = 1 - |u_k|^2 = \frac{1}{2}\left[1 + \frac{\epsilon(k)}{E(k)}\right] \tag{C3}$$

So at k_f

$$\epsilon(k_f) = 0 \tag{C4}$$
$$E_\pm(k_f) = \pm\Delta(k_f) \tag{C5}$$
$$|u_k|^2 = |v_k|^2 = \frac{1}{2} \tag{C6}$$
$$A(\boldsymbol{k_f},\omega) = \frac{\Sigma''}{2\pi}\left\{\frac{1}{[\omega - \Delta(k)]^2 + \Sigma''^2} + \frac{1}{[\omega + \Delta(k)]^2 + \Sigma''^2}\right\} = A(\boldsymbol{k_f},-\omega) \tag{C7}$$

So the effect of the Fermi distribution can be eliminated by symmetrising (including a symmetric resolution effect $R(\boldsymbol{k},\omega)$).

$$\begin{aligned} I(\boldsymbol{k},\omega) &= I_0\, A(\boldsymbol{k_f},\omega) f(\omega) * R(\boldsymbol{k},\omega) \\ &\quad + I_0\, A(\boldsymbol{k_f},-\omega) f(-\omega) * R(\boldsymbol{k},-\omega) \\ &= I_0\, (A(\boldsymbol{k_f},\omega) f(\omega) + A(\boldsymbol{k_f},\omega)[1 - f(\omega)]) * R(\boldsymbol{k},\omega) \\ &= I_0\, A(\boldsymbol{k_f},\omega) * R(\boldsymbol{k},\omega) \end{aligned}$$

Appendix D: Phenomenological Model of High-Temperature Superconductivity

Model from Norman *et al.* [52] is fit to data of symmetrised EDCs to determine the gap Δ. The self energy

$$\Sigma(\boldsymbol{k},\omega) = -i\Gamma_1 + \frac{\Delta^2}{(\omega + \epsilon(\boldsymbol{k}) + i\Gamma_0)} \tag{D1}$$

$$\Sigma(\boldsymbol{k},\omega)' = \Re(\Sigma(\boldsymbol{k},\omega));\ \Sigma(\boldsymbol{k},\omega)'' = \Im(\Sigma(\boldsymbol{k},\omega))$$

$$A(\boldsymbol{k},\omega) = \frac{1}{\pi}\frac{\Sigma''(\boldsymbol{k},\omega)}{(\omega - \epsilon(\boldsymbol{k}) - \Sigma'(\boldsymbol{k},\omega))^2 + \Sigma''(\boldsymbol{k},\omega)^2} \tag{D2}$$

Appendix E: Dosing Parameter

Using the Luttinger volume, assuming circular, double degenerate electron bands.

$$A_{e^-} = \pi k_f^2 \tag{E1}$$

$$A_{BZ} = \frac{4\pi^2}{a^2} \tag{E2}$$

$$x = 2\frac{2A_{e^-}}{A_{BZ}} \tag{E3}$$